Journal of Applied Physics

AIP Publishing

Engineering visible light emitting point defects in Zr-implanted polycrystalline AlN films

A. Aghdaei[1, 2, 3], R. Pandiyan[3], B. Ilahi[1,2,3], M. Chicoine[4], M. El Gowini[5], F. Schiettekatte[4], L. G. Fréchette[3] and D. Morris[1, 2, 3]*

AFFILIATIONS

[1] Département de physique, Regroupement québécois sur les matériaux de pointe, Faculté des sciences, Université de Sherbrooke, Québec, Canada J1K 2R1
[2] Institut quantique, Université de Sherbrooke, Québec, Canada J1K 2R1
[3] Institut Interdisciplinaire d'Innovation Technologique (3IT), Université de Sherbrooke, 3000 Blvd. Université, Sherbrooke, Québec, Canada ; Laboratoire Nanotechnologies Nanosystèmes (LN2), CNRS UMI-3463, 3000 Blvd. Université, Sherbrooke, Québec, Canada, J1K 0A5
[4] Département de Physique, Regroupement québécois sur les matériaux de pointe, Université de Montréal, C.P. 6128, Succursale Centre-Ville, Montréal, QC, Canada H3C 3J7
[5]Teledyne DALSA Semiconducteur, Bromont, Québec, Canada J2L 1S7

***Author to whom correspondence should be addressed:** Denis. Morris@USherbrooke.ca

Abstract

We have investigated the impact of thermal annealing gaseous atmosphere of argon, nitrogen and forming gas on the structural and optical properties of thin polycrystalline AlN films subjected to high-energy zirconium ions implantation. X-ray diffraction, Raman spectroscopy, scanning electron microscopy and atomic force microscopy measurements show that the structural and morphological properties of the Zr-implanted AlN films depends on the annealing gaseous environment. The post-implantation annealing under argon atmosphere yields the lowest structured surface roughness with increased grain size. Photoluminescence spectroscopy revealed multiple point defects and defect complexes related emission bands in the visible range. A series of absorption bands have been observed using photoluminescence excitation spectroscopy. The origin of the emission or absorption bands is identified and attributed to various types of point defects and defect complexes, theoretically reported for AlN. New emission and absorption peaks at 1.7 eV (730 nm) and 2.6 eV (466 nm), respectively, have been identified and attributed to the $(Zr_{Al}\text{-}V_N)^0$ defect complexes.

1.Introduction

During the last decades wide-bandgap materials like III-Nitride semiconductors and diamond attract considerable attention for their potential applications in the field of high-power electronics, photonics, sensing, and quantum information processing [1–7]. Among the III-Nitrides materials, AlN has the widest direct bandgap of (~ 6 eV) [8], high thermal conductivity (about 320 W/m·K) [8], excellent optical [9] and dielectric properties, low dielectric constant and good mechanical strength [8], negative electron affinity [10–12] and high piezoelectric coefficient [13]. These unique properties make AlN a potential candidate for optoelectronics devices [9,14,15], microelectromechanical systems (MEMS) [16], surface acoustic wave sensors (SAWs) [17] and electro-optic modulators [18].

Furthermore, point defects and defect complexes in AlN have recently received considerable attention due to their ability to act as qubits with a spin

character that can be tuned by strain engineering [19–21] and their application for the room-temperature quantum emitter [22] . Indeed, negatively charged nitrogen vacancies, group IV impurity (Ge, Sn, Ti, Zr) - vacancy pairs, and more recently large metal ion (Y, La, Zr, and Hf) - vacancy pairs in AlN, have been theoretically reported as promising qubit candidates [19–21]. These studies have shown, in particular, that the formation of Zr-vacancy pairs is energetically favorable in AlN while such defects have spin-triplet ground states with an electronic configuration similar to that of the nitrogen-vacancy centers in diamond. It is possible to generate this type of defects using a post-growth ion-implantation technique. This can be achieved firstly by bombarding a lightly Zr-doped AlN film with low-energy protons (necessary to create vacancies in the doped film) or secondly by directly implanting heavy Zr ions into an unintentionally doped film. In both cases, it is necessary to perform a post-implantation thermal annealing treatment to remove most of the implantation damage and to promote the formation of Zr-vacancy pairs. The first method requires an optimization of the deposition conditions to obtain a film with the right doping level, which has not yet been done within our group. Moreover, it is still difficult to obtain this type of film commercially. The second method, which we have advocated for this study, controls the Zr concentration via the implantation dose and the depth distribution of these atoms through the choice of implantation energies. However, the damage and defects caused by the implantation of heavy ions in the AlN film are more important. It is therefore essential to study the influence of thermal annealing conditions on the structural and optical properties of the implanted AlN films. So far, the impact of different ion species (Si, Cd, Ag, Hf and Ti) on the structural properties of ion-implanted AlN thin films have been reported [23–29], but further studies are needed to better understand the influence of thermal annealing conditions on these properties. In this work, we report on the impact of high energy implantation of Zr ions and subsequent annealing in various gaseous atmosphere on the structural and optical properties of polycrystalline AlN thin films. Ti and Hf ions can also create defect complexes of interest for quantum technologies, but we chose Zr ions for their intermediate atomic number and because, to our best knowledge, Zr-implanted AlN films have never been studied before. A special attention has been devoted to the generation, and identification of optically active point defects and defect complexes. This study paves the way to future studies exploiting these luminescent defects for example for single-photon source technologies.

2.Experimental Details

AlN thin films were deposited by a reactive DC magnetron sputtering (MS) technique on (100) oriented silicon (Si) substrate. Prior to the deposition process, the substrates were cleaned *ex-situ* using a standard RCA cleaning process carried out in two steps, called SC1 and SC2. The substrates were then rinsed with deionized water and dried under N_2 gas flow, prior to loading them in the sputtering chamber for the deposition. A commercial high purity Al disc with a diameter of 33 cm was used as a target, sputtered at 10 kW operating power. The sputtering process was carried out in an atmosphere composed of a mixture of high purity Ar and N_2 gases. The flow rates of gases were regulated by two mass flow controllers and the total gas flow rate ($Ar+N_2$) was kept constant at 70 sccm. The gas flow rates were monitored to maintain a constant pressure of 3 mTorr in the chamber during the sputter-deposition process. The substrates were radiatively heated to an on-substrate temperature of $350\,°C$ and the holder was biased negatively to $-37\,V$. The film thickness was measured using ellipsometry (Optiprime-TF system) and was found to be of 1 µm.

AlN samples of 5×5 mm^2 were cut out of an 8-inch wafer. Before implantation, the samples were carefully cleaned with acetone, isopropyl alcohol and water. Ion implantation was performed at room temperature, using Zr ions at different kinetic energies (250 keV, 1 MeV, 1.75 MeV, and 2.5 MeV). The fluence is fixed at 1×10^{14} ion/cm^2 for each energy. The depth distribution of displacement damages and Zr atoms in the host material is

estimated using SRIM 2013 [30] simulations (Figure 1).

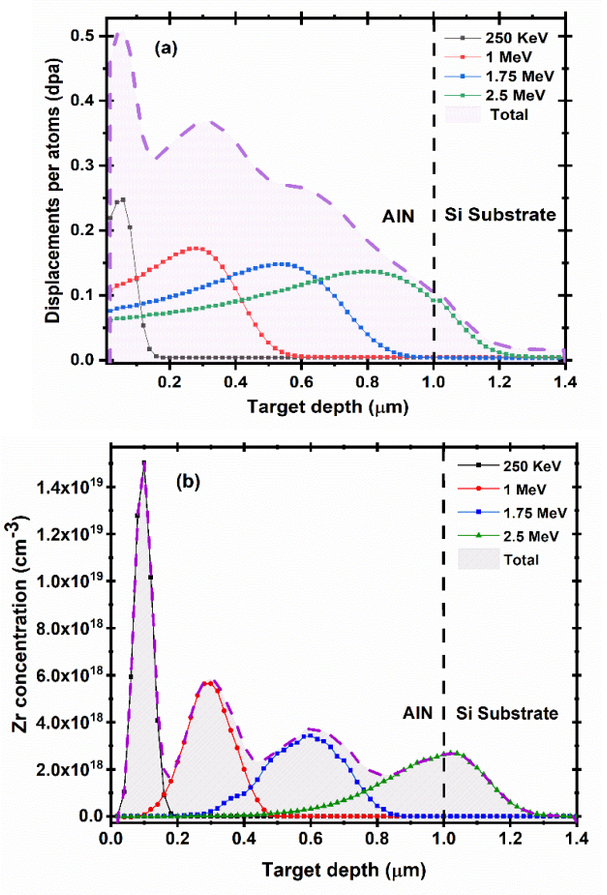

Figure 1. Depth profile of (a) displacement damage and (b) implanted ions concentration for the different ion implantation energies, according to SRIM simulations. The implantation fluence was 1 x 10^{14} ion/cm^2.

To partially repair the structural damage caused by ion bombardment, the implanted samples were annealed in a quartz tube furnace. Post-implantation annealing was performed under different atmospheres including argon, nitrogen and forming gas (FG, 95 % nitrogen + 5 % hydrogen) at 1050ºC for 1h. Since the AlN films can be easily oxidized when they are exposed to air at high temperature, we allow the samples to cool down to room temperature at a rate of 5^{0}C/min, in the furnace, keeping the same annealing gaseous atmosphere.

The samples' structural properties were characterized using a combination of techniques. The film surface morphology was assessed using a Zeiss 1540 XB scanning electron microscope (SEM) operated at 20 kV. The surface topography and root-mean-square (RMS) roughness of the films were characterized by atomic force microscopy (AFM) measurements using a Dimension Icon Bruker system in a non-contact mode. The crystalline structure of the AlN films was investigated through for $\theta - 2\theta$ scans and rocking curve measurements using a Bruker (D8 Discover Model) X-ray diffractometer with high-intensity Cu-Kα radiation ($\lambda = 1.5406$ Å) . Micro-Raman measurements were carried out at room temperature using a backscattering configuration. A Labram-800 Raman spectrometer equipped with a nitrogen-cooled charge-coupled device (CCD) was used to record the Raman spectra. A He-Ne laser of wavelength 632.8 nm was used at a constant power of 1.3 mW as the excitation source and a 50 × microscope objective was used to focus the laser beam to a spot diameter of about 3 μm on the sample surface.

The quantities of O, H and C present in the AlN samples were depth-profiled by Elastic Recoil Detection by Time-of-Flight (ERD-TOF) analysis [31] using a Co 40 MeV ion beam incident at 15° from the surface. The recoils are detected at 30° with respect to the beam axis, except H where it is at 46°, through a beam-absorbing foil. The energy spectra were converted to elemental depth profiles using Allegria software [32].

The photoluminescence (PL) spectra were obtained at room temperature using a 1m-spectrometer (SPEX model) equipped with a cooled photomultiplier tube (Hamamatsu R2658 model). A 266 nm pulsed UV laser source providing 8 mW was used as an excitation source where the excitation beam was focused onto the sample surface on a spot diameter of about 200 μm. The laser beam was nearly perpendicular to the c-plane surface of the AlN films and the PL signals were recorded using a conventional lock-in technique. Photoluminescent excitation (PLE) spectra were obtained using a 200-W Xenon lamp connected to a monochromator (Princeton Instrument SP-

Sample	c (Å)	strain (%)	Raman E_2(high) peak position (cm^{-1})	Raman E_2(high) peak width (cm^{-1})	Annealing atmosphere
As-dep AlN	4.984	0.08	659.5	16	-
Zr/AlN (as- implanted)	5.024	0.88	662.0	40	-
Zr/AlN: Ar	4.992	0.24	661.9	17	Argon
Zr/AlN: N	4.992	0.24	661.5	17	Nitrogen
Zr/AlN: FG	4.985	0.10	661.0	16	Forming gas

Table 1. Lattice parameter, c-axis strain, Raman E2(high) peak position and peak width for the different AlN films.

2300i). A second monochromator and a silicon photodiode were used for the detection of photons reemitted by the samples at specific wavelengths.

3. Results and Discussions

3.1 Structural characterization

Figure 2 shows the XRD spectra ($\theta - 2\theta$) of the as deposited AlN films Zr-implanted and after their annealing under different gaseous atmosphere at 1050 ºC for 1h. The as-deposited film presents features at 36^0 and 76.3^0 corresponding to the (0002) and (0004) AlN diffraction peaks [33]. For the Zr-implanted film (Zr/AlN), these peaks are shifted to lower diffraction angles while they return almost to their original positions after annealing. The shift of the diffraction peaks is attributed to a change in the strain amount in the AlN layer as a result of the implantation and decreases significantly upon thermal annealing. The c-lattice parameter's values can be determined from the Bragg's law and the relationship between the distance separating the $(000l)$ atomic planes and the parameter c. The strain amount in the AlN films can be determined using the expression $\frac{\Delta c}{c} = \frac{c - c_{bulk}}{c_{bulk}}$, where $c_{bulk} = 4.980$ Å [34] is the c-lattice parameter of the bulk AlN material. The values of the c-lattice parameters and the strain amount in the different AlN layers, extracted from the diffraction patterns of Figure 2, are given in Table 1.

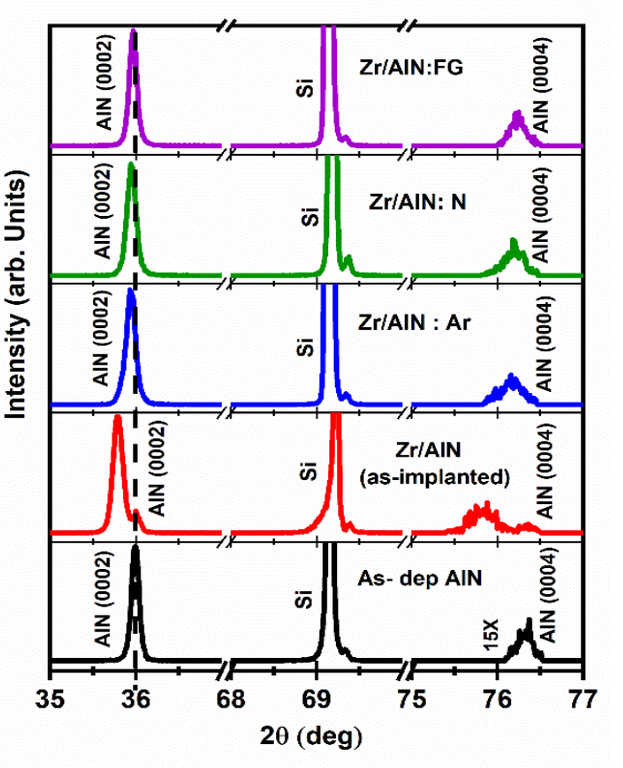

Figure 2. θ-2θ XRD patterns of the AlN films before and after Zr implantation and annealing under various atmospheres. The dashed line shows the position of the (0002) peak for the as-deposited AlN film. A peak related to the Si substrate is also shown.

For the as-deposited film, since no other peaks are observed in the XRD pattern, we conclude that the AlN polycrystalline film is purely c-axis oriented. For the sputtered films the intrinsic defects, lattice or domain mismatch and different thermal expansion coefficients are three main sources of residual stress. However, as reported by J.X. Zhang et al. the large lattice mismatch (42.7%) between AlN films and Si (001) substrate is the main contribution for the internal stress in the formed film [35]. Partial strain relaxation in the AlN layer is usually realized by the generation of interface steps and dislocations at the AlN/Si interface[36]. XRD measurements show that the residual amount of strain along the c-axis of this film is about 0.08%.

For the as-implanted film (Zr/AlN), the amount of strain induced in the c-axis direction reaches a value of 0.88%. A similar behavior, resulting from the implantation induced damage, has been observed for ion-implanted GaN films [37]. The low intensity peaks observed at 36° and 76.3°, corresponding to the diffraction peaks of the as-deposited film, indicates that a small fraction of the film retains its structural properties even after ion-implantation. For post-implantation annealed samples, the strain along the c-axis slightly depends on the thermal annealing conditions with values ranging from 0.10% to 0.24%. The (0002) and (0004) diffraction peaks are narrower than those of the Zr- implanted sample but wider than those of the as-deposited films. This behavior indicates that the crystalline quality of the film is partially restored after the thermal annealing treatment. The influence of the annealing gas atmosphere on the width (FWHM) of the XRD peaks is best illustrated using ω-scans. The XRD rocking curves of the AlN films annealed under Ar, N_2 and FG are shown in Figure 3, for a detector position centered on the AlN (0002) peak. The rocking curve of the as-deposited film is also shown for comparison. The values of the full width at half maximum (FWHM) of these peaks are also indicated in Figure 3. The broadening of the XRD peaks results from both size and strain fluctuations in the various AlN crystallites forming the film, as well as amorphous zones in the as-implanted sample. The results show that the thermal annealing performed under a forming gas atmosphere is the most effective treatment to restore the crystalline quality of the implanted film.

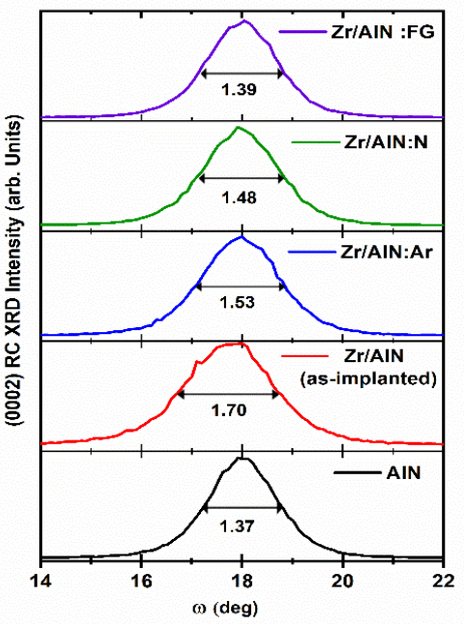

Figure 3. (0002) XRD rocking curves of the annealed AlN films using different gas atmospheres (Ar, N_2 and FG). The rocking curve of the as-deposited film is shown for comparison.

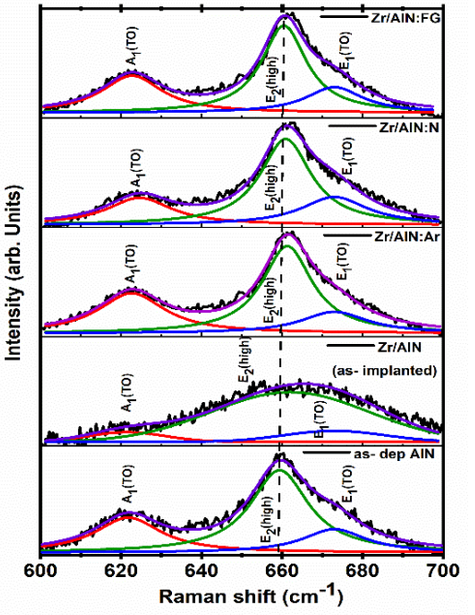

Figure 4. Raman spectra of the annealed AlN films using different gas atmospheres (Ar, N_2 and FG). The Raman spectra of the as-deposited and the as-implanted AlN films are shown for comparison. The dashed line shows the position of the E_2(high) vibrational mode for the as-deposited film.

Figure 4 illustrates the Raman spectra of the annealed AlN films using different gas atmosphere (FG, N_2 and Ar). The Raman spectra of the as-deposited and the as-implanted AlN films are shown for comparison. The laser excitation power of 1.3 mW is low enough to avoid sample heating. The spectra can be reproduced by a sum of the three broadened peaks, corresponding to the active Raman vibration modes of the wurtzite structure of the AlN crystal: namely the A_1(TO), E_2(high) and E_1(TO) modes [38]. There are different broadening mechanisms already observed for crystalline AlN and thin film of AlN nanocrystallites. These include: i) inhomogeneous broadening mechanisms due to strain fluctuations in the layer [39], ii) asymmetric line shape features caused by crystallite size effects on the $q \neq 0$ allowed modes and on the phonon dispersion relation [40,41], and iii) homogeneous broadening mechanisms related to the finite phonon lifetime related to the phonon interaction with the crystallite boundaries [42]. Different fit functions (Gaussian, Lorentzian or Voigt) have been used in the literature [35, 37–39], but since we are interested in the effect of the fabrication process (ion implantation + annealing) on the position of the different allowed Raman modes and their related peak linewidths, we have simplified the analysis by using a sum of Lorentzian functions for each sample's spectrum, except for the Zr/AlN sample which shows a clear gaussian spectral line shape. The positions of these peaks are compatible with reported values for the w-AlN crystal [44–46]. For the as-implanted sample, heavy ion implantation in covalently bond materials usually results in the formation of amorphous zones featuring wider distribution of bond angle and interatomic distances than in the crystal that lift the selection rules and result in much broader Raman peaks [47], as observed in Fig. 4 and Table 1. For the annealed samples, the width of the main Raman peak, associated with the E_2(high) mode, comes back to its initial value, in the as-deposited film. This is consistent with a restored crystalline quality for the samples annealed in Ar , N and FG atmosphere. This peak is also slightly shifted towards higher frequencies, compared to that of the as-deposited sample. The observed shifts are about 2.4, 1.9 and 2 cm^{-1} for samples annealed under an atmosphere of Ar, N_2 and FG, respectively. These Raman shifts are consistent with the amount of residual strain values in these films, deduced from the XRD measurements.

Figure 5 shows the ERD-TOF depth profiles of O, H and C elemental species, for the different AlN films. According to the lattice parameters we found by XRD and knowing their composition, the density of our films is 9.5×10^{22} at/cm^3. Hence, the depth scale in these graphs corresponds approximately to nm. It is worth pointing out the depth profiles cover only about 1/10 of the film thickness, near the surface. The C content is below 0.4% in all films and extends through the layer. It remains about the same of all samples. These are indications that it was introduced during the deposition process, probably as a result of low levels of organic molecules contamination in the deposition chamber. However, there is no excess C peak on the surface of the films, so post-treatments do not introduce additional C contamination. The H content is below 0.6% for all films, except for the film annealed under FG atmosphere, where a constant value of ~ 0.9% is reached. Hydrogen typically favors the passivation of dangling bonds.

All films present an O content near the surface, which extends about 20×10^{16} at/cm^2 in depth, which corresponds to ~ 20 nm. For the as-deposited film, the O content reaches about 13% at this free surface. Given the nanostructure of the films (see below), the incident ions hit the surface at various angles during the ERD-TOF measurement, resulting in a broadening of surface peaks. This depth profile is therefore compatible with the formation of a native aluminum oxide (Al_2O_3) on the surface of the film, which is typically up to 10 nm thick for pure Al. Despite the low oxygen content in the furnace, thermal

annealing under Ar or N_2 atmosphere promotes the incorporation of oxygen at the surface and in the AlN film, in which case it is detectable at ~1% levels at depth of up to 150-200 nm in these films. While inherently quantitative, ERD-TOF sensitivity is limited to ~0.1%. Some O contamination is probably present deeper in the sample given its high reactivity to Al.

It is interesting to note that the O-profile for the annealed film under the FG atmosphere is almost identical to that of the as-deposited and as-implanted films. It thus seems that the H passivation of the dangling bonds limits the incorporation or diffusion of O in the film. According to our interpretation, this surface passivation phenomenon can also influence the residual strain in the film. Indeed, limiting the oxygen content in the AlN film during thermal annealing should promote the transfer of Zr interstitials into substitutional sites (Zr_{Al}) and thus reduce the internal strain, consistent with the micro-Raman and XRD results. Otherwise, the formation of V_{AL}-O_N defect complexes is favored over substitutional Zr_{Al} defects, as predicted by DFT calculations [19–21].

Figure 6 shows the SEM and AFM topographical images of the different AlN films. The morphology of the as-deposited film was quite uniform and dense with a mean surface grain diameter of 41 nm and a RMS surface roughness of 1.5 nm. The ion implantation process alone does not noticeably alter the film morphology. Larger and relatively flat polycrystalline flakes (grain size > 59 nm and RMS surface roughness of ~ 0.91 nm) are found on the surface of the films annealed under an atmosphere of Ar and N. A summary of the statistical values of RMS surface roughness and grain size are given in Figure 7, for all samples. The reorganization of atoms on the film surface is governed by thermal activation process. Higher number of dangling bonds help diffusion and reorganization of the atoms on the surface of these films, resulting in larger grains. For the film annealed under the FG atmosphere, the H-passivation of these bonds hampers these mechanisms and help preserve the as-deposited structure.

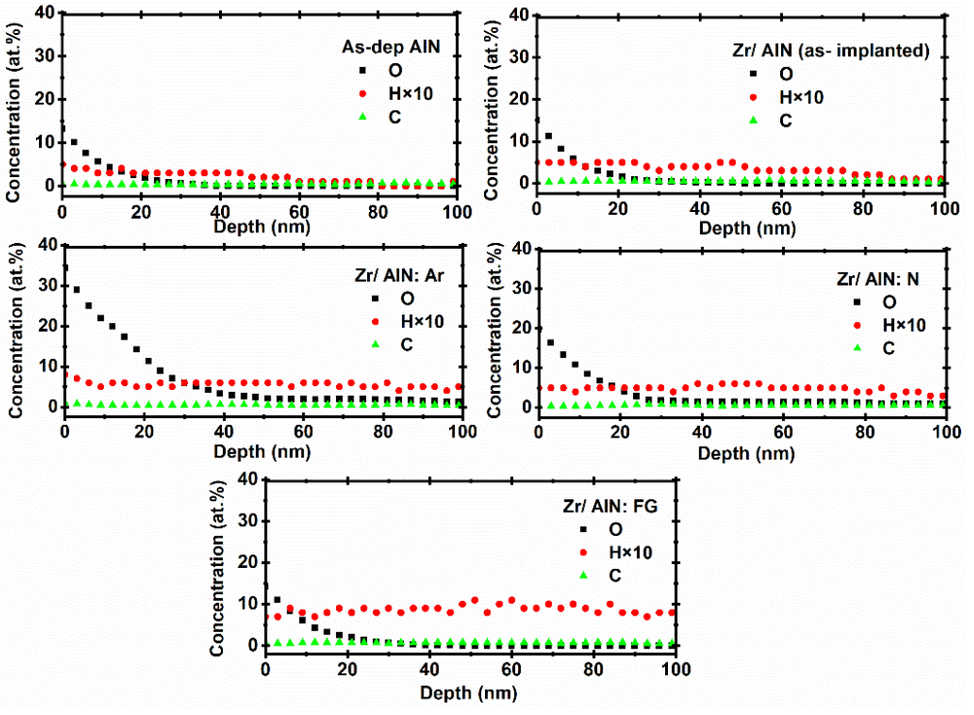

Figure 5. ERD-TOF depth profiles of O, H and C elemental species, for the different AlN films.

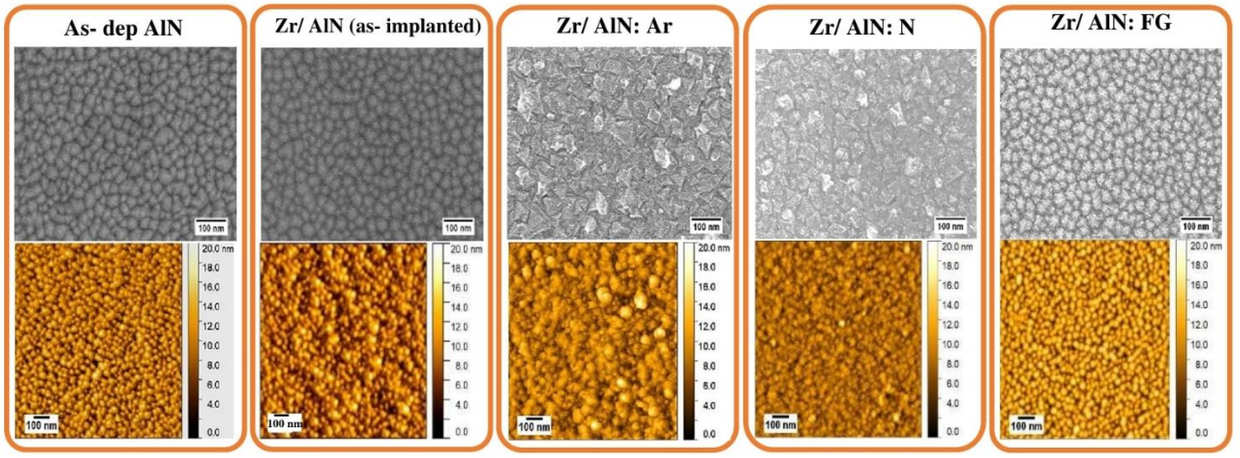

Figure 6. SEM micrographs (top) and AFM images (bottom) of the different AlN films

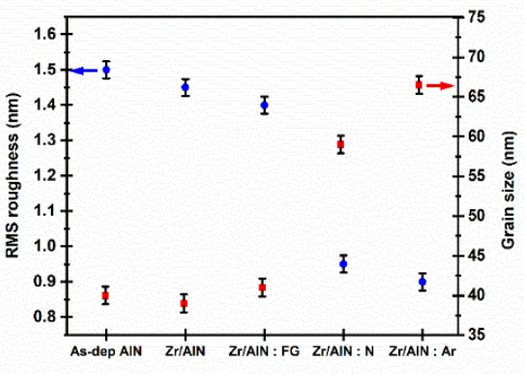

Figure 7. Summary of the statistical values of surface roughness and grain size extracted from the analysis of the SEM and AFM images of Fig. 6.

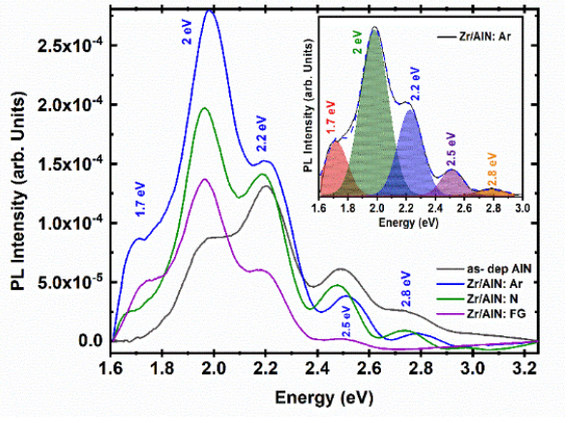

Figure 8. Room-temperature PL spectra of the different AlN thin films. The insert shows the best fitting curve of the PL spectrum of the Zr/AlN: Ar film, obtained using a sum of five Gaussian-like emission bands.

3.2 Optical characterization

The influence of ion implantation and thermal annealing process on the optical properties of AlN thin films were investigated using PL and PLE spectroscopies. Figure 8 shows the PL spectra of the different AlN films, except for the as-implanted film which shows a very weak PL signal due to amorphization and the presence of a large density of non-radiative recombination centers. Spectra of Fig. 8 show the presence of several emission bands in the visible range, between 420 nm and 770 nm. The different spectra can be reproduced using a sum of up to five Gaussian-like emission bands, centered around 1.7 eV, 2 eV, 2.2 eV, 2.5 eV and 2.8 eV. The insert in Figure 8, shows the best fitting curve of the Zr/AlN: Ar PL spectrum, obtained using a sum of five Gaussian-like emission bands.

Further discussion of the influence of the fabrication process on the different defects that may exist in our AlN films has to be given, before interpreting the different PL features. Heavy ion bombardment creates a high density of amorphous zones and point defect clusters. Upon annealing, this usually results in a zoo of point defect complexes with complicated annealing dynamics [48]. In addition to the point defects, the O impurities incorporated during the deposition

process, mainly exists in the form of substitutional atom on N sites (O_N). ERD-TOF results indicates non-negligible amount of C through the layers. However, according to the literatures, the C-related levels are in 4-6 eV range, which is far from the area of our PL study [49–51]. Therefore, we do not study the C-related defects in this paper. Also, as a result of the implantation, Zr atoms can substitute other atoms of the lattice structure (Zr_{Al}), acting as point defects and/or defect complexes such as vacancy-interstitial aggregates. The non-homogeneous distribution of these defect complexes may result in a large fluctuation of the internal strain in the implanted layer. Thermal annealing promotes the displacement of vacancies and atoms to reduce the overall strain in the film. This can be accomplished in several ways: i) annihilation of vacancies with Al and N interstitials, ii) annihilation of vacancies by the transformation of O and Zr interstitials into substitutional defects, iii) formation of complex vacancy-substitutional impurity such as V_{Al}-O_N complexes and iv) dissociation of vacancies – interstitials aggregates. Up to date, the energies of formation and dissociation of these point defects and defect complexes are still poorly known in AlN. Meanwhile, ab-initio calculations using the DFT method can nevertheless be used to predict the existence of the defects most likely to form. These theoretical studies[19–21], notably predicts a lower formation energy for the V_{Al}-O_N complex compared to that of the Zr_{Al} substitutional defect. This may help understanding the influence of the annealing conditions on the relative intensity of the different emission bands, as will be seen later.

Theoretical and experimental results showed that V_N and V_{Al} point defects have shallow energy levels below the conduction band and above the valence band extrema, respectively[52,53]. Oxygen substitutional defect (O_N) and their related defect complexes, such as $V_{Al} – O_N$, have also been reported as an important defect in AlN [54–58]. Based on these studies and other DFT calculations [19–21,59], the suggested origin of the different emission bands is given in Table 2 showing also the optical transition schemes involving these most common defects. The experimental evidence and identification of most of the absorption energy levels and some of the emission energy levels, has not been yet experimentally presented. The emission band appearing around 2.8 eV can be attributed to transitions from the V_{Al} levels to the valence band (VB) [59,60]. The AlN bandgap energy is sensitive to the internal strain, as reported by H. Seo et al. [19]. This is most likely the origin of the slight shift of emission band at 2.8 eV, observed from one sample to the other in accordance with the strain variation revealed by XRD and Raman measurements. The second higher energy emission band, centered at ~ 2.5 eV, is associated with transitions from the ($V_{Al} – O_N$) levels to the VB [61]. There is also a slight shift in this band, from one sample to another, which can still be associated with changes in the internal strain in the films. The emission bands at 2.2 eV and around 2.0 eV can be associated to the $V_N \rightarrow (V^{3-}_{Al}–3O_N)$ transitions [62]) and to the emission related to ($V_{Al}–O_N$) energy levels [63], respectively. These four emission bands, between 1.9 eV and 2.9 eV, are present in the spectra of all samples, except the 2.8 eV band that seems to quench upon annealing under a forming gas atmosphere. Indeed, the annealing under a Forming gas might promote the incorporation of the Zr atoms into substitutionnel sites (Zr_{Al}) which reduce the number of V_{Al} sites resulting in significant decrease of corresponding emission intensity in Zr/AlN :FG sample.

Suggestions transitions	Absorption/ Emission	Energy (eV) (previous works)	Reference	Energy (eV) Expt. (this work)
$VB \rightarrow V_{Al}$	Absorption	3.4	[59]	3.2
$(V_{Al}–O_N)^{2-}+V_N^{+} \rightarrow (V_{Al}–O_N)^{-}+V_N^{0}$	Absorption	3.03	[59]	3.0
$(V^{3-}_{Al}–V^{+}_{N}) \rightarrow (V^{2-}_{Al}–V^{0}_{N})$	Absorption	2.49	[59]	2.7
$(Zr_{Al}\text{-}V_N)^0$	Absorption	2.83	[21]	2.6
$V_{Al} \rightarrow VB$	Emission	2.77, 2.78	[59,60]	2.8
$(V_{Al}–O_N) \rightarrow VB$	Emission	2.53	[61]	2.5
$V_N \rightarrow (V_{Al}–O_N)$	Emission	2.16	[62]	2.2
$(V_{Al}–O_N)$	Emission	2.05	[63]	2.0
$(Zr_{Al}\text{-}V_N)^0$	Emission	1.91	[21]	1.7

Table 2. Suggested transitions for absorption and emission bands seen between 1.7 and 3.25 eV.

The most striking results are the increase in the intensity of the emission band peaked at 2 eV and the appearance of a new emission band at 1.7 eV, after the post-implantation annealing treatment. The enhancement of the PL intensity at 2 eV is explained by an increase in the density of the V_{Al}-O_N defect complexes, while the appearance of a new emission band at 1.7 eV would be due to the formation of Zr_{Al}-V_N defect complexes. However, the transition energy associated with later defect complexes in strain-free AlN, has been predicted by Varley et al.[21], around 1.9 eV. The position of our emission band at 1.7 eV seems to be redshifted by the residual strain in the AlN film. Optical experiments in the presence of external stress will be required to confirm this interpretation. In comparison with other samples, the Zr/AlN:Ar shows the most intense and resolved emission peaks. Therefore, we will focus on this sample for deeper analysis on the origin of the transition energy by PLE. Absorption spectroscopy measurements are very useful for confronting experimental results with theoretical predictions. Figure 9 shows the PLE spectra of the Zr/AlN:Ar film, detected at the energy position of the main emission bands at 1.7 eV, 2 eV, 2.2 eV and 2.5 eV.

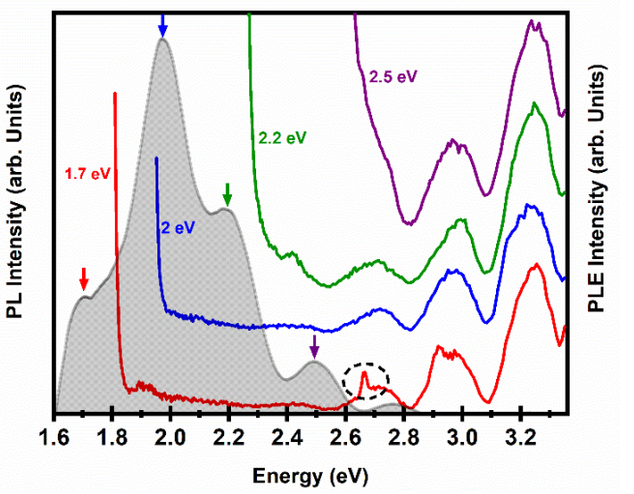

Figure. 9 Photoluminescence spectrum (shaded surface) and photoluminescence excitation spectra (colored solid lines) of the Zr-implanted and Ar-annealed AlN film. The PL spectrum is obtained using a laser source at 266 nm and the PLE spectra are obtained using a wavelength tunable source and a detection at specific energies, indicated by the colored arrows on the PL spectrum.

The three emission bands at higher energy appear to be correlated with three main absorption bands, peaked at 2.7 eV, 3.0 eV and 3.2 eV. Hybride functional calculation [59] predicted that the isolated aluminum vacancies are responsible for the absorption band around 3.4 eV. The observed absorption band at 3.2 eV might be related to this $VB \rightarrow V_{Al}$ optical transition. For the 3 eV absorption band it might originate form the charge transfer between a $(V_{Al}^{3-} - O_N)^{2-}$ complex defect and a V_N^{+} in

its vicinity, as predicted by DFT calculations [59]. The absorption band at 2.5 eV is most likely related to optical transitions involving the V_{Al} in a 3- charge state and V_N in a + charge state ($V_{Al}^{3-}+V_N^{+}\rightarrow V_{Al}^{2-}+V_N^{0}$) [59]. The slight shift of ~ 200 meV observed between experimental and theoritical predictions might originate from the residual strain in the AlN films. Finally, the PLE spectrum detected at the 1.7 eV emission band shows at additional narrow absorption band at 2.6 eV. This narrow band is very likely related to $(Zr_{Al}\ -V_N)^0$ defects [21], that has been theoretically expected to have a S=1 spin character. There has not been a previous experimental report for Zr related defects in AlN. However further experiment is necessary to investigate the spin character of these defects.

4. Conclusion

In summary, we have investigated the effect of Zr implantation and thermal annealing under different gas atmospheres on the structural and optical properties of polycrystalline AlN films. Results show that, after annealing under Ar and N atmosphere, samples show a higher amount of strain in comparison with the as-deposited AlN. These results could be interesting for strain engineering of AlN. Moreover, after annealing under the forming gas atmosphere, the results indicate a nearly full implantation damage recovery of the AlN film. Different emission and absorption bands related to complex defects are identified by PL and PLE measurements. Our ion implantation and annealing process gives rise to the formation of a new defect in AlN with emission and absorption energy at 1.7 eV and 2.6 eV respectively. These energies could be assigned to $(Zr_{Al}\ V_N)^0$ defect levels, as predicted by first-principles calculations based on density functional theory (DFT). Proton implantation in Zr-doped AlN films could also be considered in our future work as an alternative method to generate optically active Zr-vacancy pairs while minimizing the density of non-radiative recombination centers in the host crystal. This technique and such defects are potentially interesting for quantum technology applications.

Acknowledgments

This work is financed by the National sciences and engineering council of Canada (NSERC), the Canada foundation for innovation (CFI), the Fonds de recherche du Québec – Nature et technologies (FRQNT) and the Canada First Research Excellence Fund (CFREF). Thanks to Teledyne Dalsa for their expertise and for providing us with high quality AlN films. The authors would like to thank also M. Dion for his support with XRD measurements, P.L Karsenti for his support with PLE measurements, G. Laliberté for his technical support in the PL laboratory, and L. Godbout for his help with the maintenance and operation of the ion accelerator.

Data Availability

The data that support the findings of this study are available from the corresponding author upon reasonable request.

References

1. Doherty LC MW, Manson, NB, Delaney, P, Jelezko, F, Wrachtrup, J Hollenberg. The nitrogen-vacancy colour centre in diamon. Phys Rep. 2013;528(1):1–45.

2. Bucher DB, Craik DPA, Backlund MP, Turner MJ, Dor OB, Glenn DR, et al. Quantum diamond spectrometer for nanoscale NMR and ESR spectroscopy. Nat Protoc. 2019;1–41.

3. Degen CL, Reinhard F, Cappellaro P. Quantum sensing. Rev Mod Phys. 2017;89(3):035002.

4. Childress L, Hanson R. Diamond NV centers for quantum computing and quantum networks. MRS Bull. 2013;38(2):134–138.

5. Oder T, Shakya J, Lin J, Jiang H. III-nitride photonic crystals. Appl Phys Lett. 2003;83(6):1231–1233.

6. Tansu N, Zhao H, Liu G, Li X-H, Zhang J, Tong H, et al. III-nitride photonics. IEEE Photonics J. 2010;2(2):241–248.

7. Li J, Lin J, Jiang H. Growth of III-nitride photonic structures on large area silicon substrates. Appl Phys Lett. 2006;88(17):171909.

8. Strite S, Morkoç H. GaN, AlN, and InN: a review. J Vac Sci Technol B Microelectron Nanometer Struct Process Meas Phenom. 1992;10(4):1237–1266.

9. Taniyasu Y, Kasu M, Makimoto T. An aluminium nitride light-emitting diode with a wavelength of 210 nanometres. Nature. 2006;441(7091):325–328.

10. Nemanich R, Baumann P, Benjamin M, King S, Van der Weide J, Davis R. Negative electron affinity surfaces of aluminum nitride and diamond. Diam Relat Mater. 1996;5(6–8):790–796.

11. Benjamin M, Wang C, Davis R, Nemanich R. Observation of a negative electron affinity for heteroepitaxial AlN on α (6H)-SiC (0001). Appl Phys Lett. 1994;64(24):3288–3290.

12. Wu C, Kahn A, Hellman E, Buchanan D. Electron affinity at aluminum nitride surfaces. Appl Phys Lett. 1998;73(10):1346–1348.

13. Karabalin R, Matheny M, Feng X, Defaÿ E, Le Rhun G, Marcoux C, et al. Piezoelectric nanoelectromechanical resonators based on aluminum nitride thin films. Appl Phys Lett. 2009;95(10):103111.

14. Zhao Q, Zhang H, Xu X, Wang Z, Xu J, Yu D, et al. Optical properties of highly ordered AlN nanowire arrays grown on sapphire substrate. Appl Phys Lett. 2005;86(19):193101.

15. Zhao S, Connie A, Dastjerdi M, Kong X, Wang Q, Djavid M, et al. Aluminum nitride nanowire light emitting diodes: Breaking the fundamental bottleneck of deep ultraviolet light sources. Sci Rep. 2015;5:8332.

16. Piazza G, Stephanou PJ, Pisano AP. Piezoelectric aluminum nitride vibrating contour-mode MEMS resonators. J Microelectromechanical Syst. 2006;15(6):1406–1418.

17. Le X, Liu Y, Peng L, Pang J, Xu Z, Gao C, et al. Surface acoustic wave humidity sensors based on uniform and thickness controllable graphene oxide thin films formed by surface tension. Microsyst Nanoeng. 2019;5(1):1–10.

18. Xiong C, Pernice WH, Tang HX. Low-loss, silicon integrated, aluminum nitride photonic circuits and their use for electro-optic signal processing. Nano Lett. 2012;12(7):3562–3568.

19. Seo H, Govoni M, Galli G. Design of defect spins in piezoelectric aluminum nitride for solid-state hybrid quantum technologies. Sci Rep. 2016;6(1):1–10.

20. Seo H, Ma H, Govoni M, Galli G. Designing defect-based qubit candidates in wide-gap binary semiconductors for solid-state quantum technologies. Phys Rev Mater. 2017;1(7):075002.

21. Varley J, Janotti A, Van de Walle C. Defects in AlN as candidates for solid-state qubits. Phys Rev B. 2016;93(16):161201.

22. Bishop SG, Hadden JP, Alzahrani FD, Hekmati R, Huffaker DL, Langbein WW, et al. Room-Temperature Quantum Emitter in Aluminum Nitride. ACS Photonics. 2020 Jun 29;acsphotonics.0c00528.

23. Wesch W, Wendler E, Götz G, Kekelidse NP. Defect production during ion implantation of

various $A_{III}B_{V}$ semiconductors. J Appl Phys. 1989 Jan 15;65(2):519–26.

24. Lorenz K, Vianden R. Defect Recovery in AlN and InN after Heavy Ion Implantation. Phys Status Solidi C. 2003;0(1):413–6.

25. Wendler E, Wesch W, Götz G. Defects in Weakly Damaged Ion-Implanted GaAs and Other III–V Semiconductors. Phys Status Solidi A. 1989 Mar 16;112(1):289–99.

26. Miranda SMC, Kessler P, Correia JG, Vianden R, Johnston K, Alves E, et al. Ion implantation of Cd and Ag into AlN and GaN. Phys Status Solidi C. 2012 Mar;9(3–4):1060–4.

27. Borowski M, Traverse A, Dallas JP. Structural characterization of Ti implanted A1N. J Mater Res. 1995;10(12):7.

28. Kanechika M, Kachi T. n-type AlN layer by Si ion implantation. Appl Phys Lett. 2006 May 15;88(20):202106.

29. Miranda SMC, Franco N, Alves E, Lorenz K. Cd ion implantation in AlN. Nucl Instrum Methods Phys Res Sect B Beam Interact Mater At. 2012 Oct;289:43–6.

30. James F. ZieglerJochen P. Biersack. Stopping and Range of Ions in Matter. Pergamon. New York; 1985.

31. Chicoine M, Schiettekatte F, Laitinen MI, Sajavaara T. Oxy-nitrides characterization with a new ERD-TOF system. Nucl Instrum Methods Phys Res Sect B Beam Interact Mater At. 2017 Sep;406:112–4.

32. Schiettekatte F, Chicoine M, Gujrathi S, Wei P, Oxorn K. Allegria: a new interface to the ERD program. Nucl Instrum Methods Phys Res Sect B Beam Interact Mater At. 2004 Jun;219–220:125–9.

33. Khan S, Shahid M, Mahmood A, Shah A, Ahmed I, Mehmood M, et al. Texture of the nano-crystalline AlN thin films and the growth conditions in DC magnetron sputtering. Prog Nat Sci Mater Int. 2015 Aug;25(4):282–90.

34. Nilsson D, Janzén E, Kakanakova-Georgieva A. Lattice parameters of AlN bulk, homoepitaxial and heteroepitaxial material. J Phys Appl Phys. 2016 May 5;49(17):175108.

35. Zhang JX, Cheng H, Chen YZ, Uddin A, Yuan S, Geng SJ, et al. Growth of AlN films on Si (100) and Si (111) substrates by reactive magnetron sputtering. Surf Coat Technol. 2005 Aug;198(1–3):68–73.

36. Wang W, Yang W, Liu Z, Wang H, Wen L, Li G. Interfacial reaction control and its mechanism of AlN epitaxial films grown on Si(111) substrates by pulsed laser deposition. Sci Rep. 2015 Sep;5(1):11480.

37. Pipeleers B, Hogg SM, Vantomme A. Defect accumulation during channeled erbium implantation into GaN. J Appl Phys. 2005;98(12):123504.

38. Prokofyeva T, Seon M, Vanbuskirk J, Holtz M, Nikishin SA, Faleev NN, et al. Vibrational properties of AlN grown on (111)-oriented silicon. Phys Rev B. 2001 Mar 7;63(12):125313.

39. Lughi V, Clarke DR. Defect and stress characterization of AlN films by Raman spectroscopy. Appl Phys Lett. 2006 Dec 11;89(24):241911.

40. Yogi P, Saxena SK, Mishra S, Mishra V, Rai HM, Late R, et al. Interplay between Phonon Confinement and Fano Effect on Raman line shape for semiconductor nanostructures: Analytical study. Solid State Commun. 2016 Mar;230:25–9.

41. Gao Y, Yin P. Origin of asymmetric broadening of Raman peak profiles in Si nanocrystals. Sci Rep. 2017 Apr;7(1):43602.

42. Bergman L, Alexson D, Murphy PL, Nemanich RJ, Dutta M, Stroscio MA, et al. Raman analysis of phonon lifetimes in AlN and GaN of wurtzite structure. Phys Rev B. 1999 May 15;59(20):12977–82.

43. Wang J, Chen D, Xu Y, Liu Q, Zhang L. Influence of the Crystal Texture on Raman

Spectroscopy of the AlN Films Prepared by Pulse Laser Deposition. J Spectrosc. 2013;2013:1–6.

44. Kuball M, Hayes J, Prins A, Van Uden N, Dunstan D, Shi Y, et al. Raman scattering studies on single-crystalline bulk AlN under high pressures. Appl Phys Lett. 2001;78(6):724–726.

45. Liu MS, Nugent K, Prawer S, Bursill L, Peng J, Tong Y, et al. Micro-Raman scattering properties of highly oriented AlN films. Int J Mod Phys B. 1998;12(19):1963–1974.

46. McNeil LE, Grimsditch M, French RH. Vibrational spectroscopy of aluminum nitride. J Am Ceram Soc. 1993;76(5):1132–1136.

47. Roorda S, Sinke WC, Poate JM, Jacobson DC, Dierker S, Dennis BS, et al. Structural relaxation and defect annihilation in pure amorphous silicon. Phys Rev B. 1991 Aug 15;44(8):3702–25.

48. Béland LK, Anahory Y, Smeets D, Guihard M, Brommer P, Joly J-F, et al. Replenish and Relax: Explaining Logarithmic Annealing in Ion-Implanted c -Si. Phys Rev Lett. 2013 Sep 4;111(10):105502.

49. Nagashima T, Kubota Y, Kinoshita T, Kumagai Y, Xie J, Collazo R, et al. Structural and Optical Properties of Carbon-Doped AlN Substrates Grown by Hydride Vapor Phase Epitaxy Using AlN Substrates Prepared by Physical Vapor Transport. Appl Phys Express. 2012 Nov 12;5(12):125501.

50. Gaddy BE, Bryan Z, Bryan I, Xie J, Dalmau R, Moody B, et al. The role of the carbon-silicon complex in eliminating deep ultraviolet absorption in AlN. Appl Phys Lett. 2014 May 19;104(20):202106.

51. Collazo R, Xie J, Gaddy BE, Bryan Z, Kirste R, Hoffmann M, et al. On the origin of the 265 nm absorption band in AlN bulk crystals. Appl Phys Lett. 2012 May 7;100(19):191914.

52. Laaksonen K, Ganchenkova M, Nieminen R. Vacancies in wurtzite GaN and AlN. J Phys Condens Matter. 2008;21(1):015803.

53. Schulz T, Albrecht M, Irmscher K, Hartmann C, Wollweber J, Fornari R. Ultraviolet luminescence in AlN. Phys Status Solidi B. 2011;248(6):1513–1518.

54. Spiridonov D, Weinstein I, Vokhmintsev A, Beketov A. Cathodoluminescence of oxygen-vacancy centers in structures of aluminum nitride. Bull Russ Acad Sci Phys. 2015;79(2):211–214.

55. Kazan M, Rufflé B, Zgheib C, Masri P. Oxygen behavior in aluminum nitride. J Appl Phys. 2005;98(10):103529.

56. Mattila T, Nieminen RM. Ab initio study of oxygen point defects in GaAs, GaN, and AlN. Phys Rev B. 1996;54(23):16676.

57. Slack GA, Schowalter LJ, Morelli D, Freitas Jr JA. Some effects of oxygen impurities on AlN and GaN. J Cryst Growth. 2002;246(3–4):287–298.

58. Uedono A, Ishibashi S, Keller S, Moe C, Cantu P, Katona T, et al. Vacancy-oxygen complexes and their optical properties in AlN epitaxial films studied by positron annihilation. J Appl Phys. 2009;105(5):054501.

59. Yan Q, Janotti A, Scheffler M, Van de Walle CG. Origins of optical absorption and emission lines in AlN. Appl Phys Lett. 2014;105(11):111104.

60. Sedhain A, Du L, Edgar JH, Lin J, Jiang H. The origin of 2.78 eV emission and yellow coloration in bulk AlN substrates. Appl Phys Lett. 2009;95(26):262104.

61. Hu H, Ji X, Wu Z, Yan P, Zhou H, Du S, et al. Synthesis and photoluminescence of AlN: Mn hexagonal maze-like complex nanostructure. Mater Lett. 2012;70:34–36.

62. Tang Y, Cong H, Li F, Cheng H-M. Synthesis and photoluminescent property of AlN

nanobelt array. Diam Relat Mater. 2007;16(3):537–541.

63. Lamprecht M, Jmerik VN, Collazo R, Sitar Z, Ivanov SV, Thonke K. Model for the deep defect-related emission bands between 1.4 and 2.4 eV in AlN: Deep defect-related emission bands between 1.4 and 2.4 eV. Phys Status Solidi B. 2017 Aug;254(8):1600714.

AIP Publishing

Journal of Applied Physics

ACCEPTED MANUSCRIPT

This is the author's peer reviewed, accepted manuscript. However, the online version of record will be different from this version once it has been copyedited and typeset.
PLEASE CITE THIS ARTICLE AS DOI: 10.1063/5.0030221

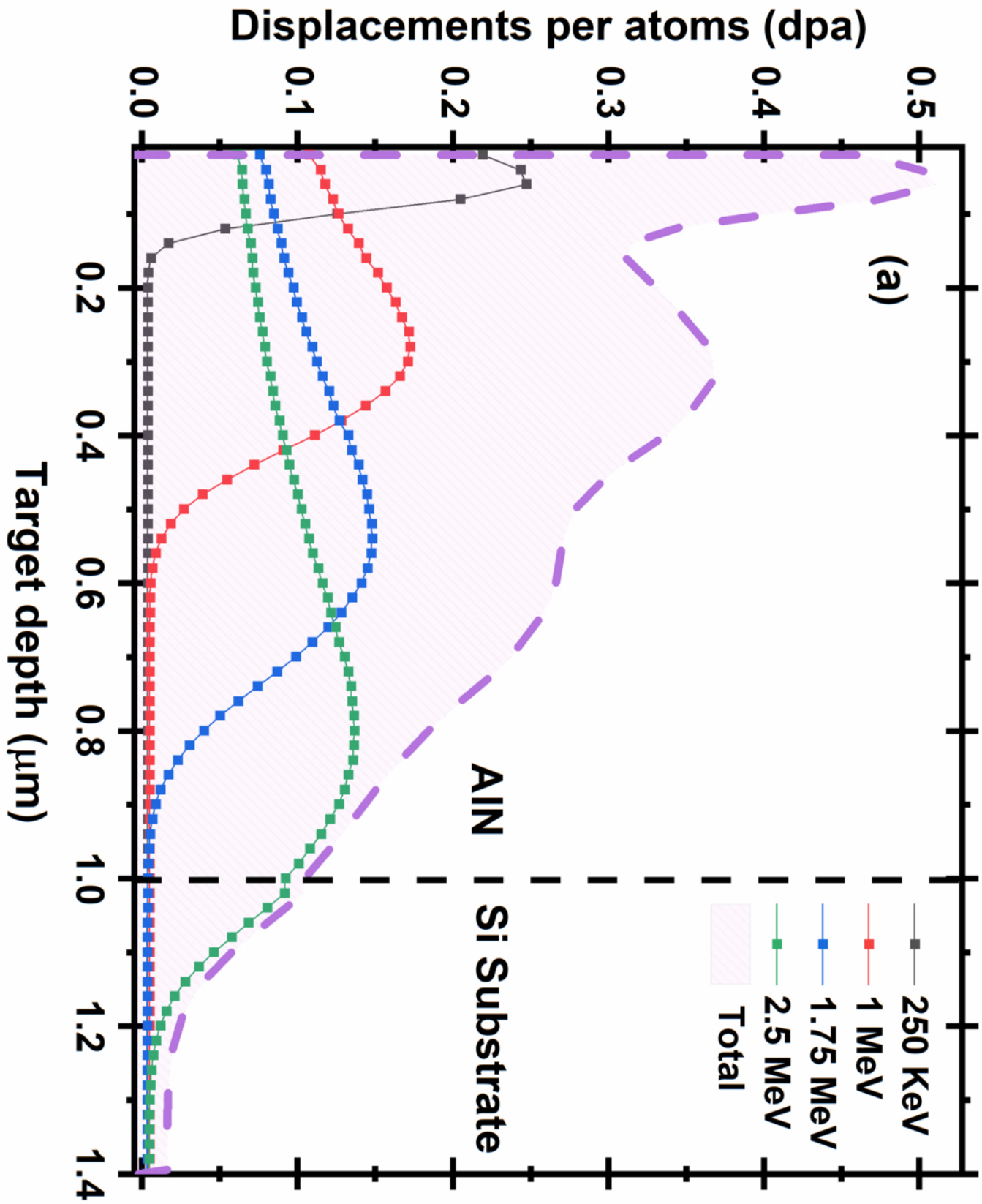

Journal of Applied Physics

PLEASE CITE THIS ARTICLE AS DOI: 10.1063/5.0030221

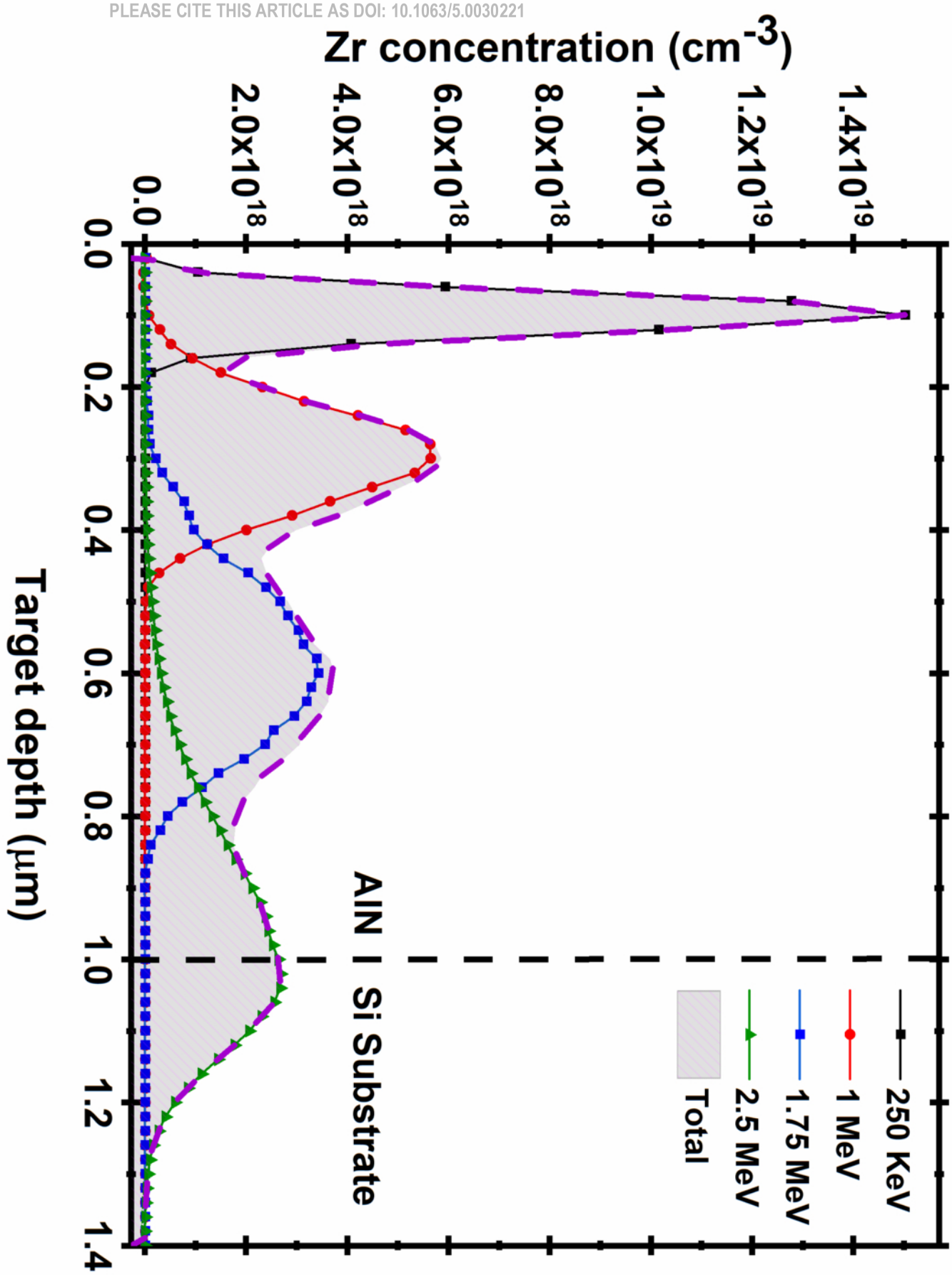

AIP Publishing

Journal of Applied Physics

ACCEPTED MANUSCRIPT

This is the author's peer reviewed, accepted manuscript. However, the online version of record will be different from this version once it has been copyedited and typeset.
PLEASE CITE THIS ARTICLE AS DOI: 10.1063/5.0030221

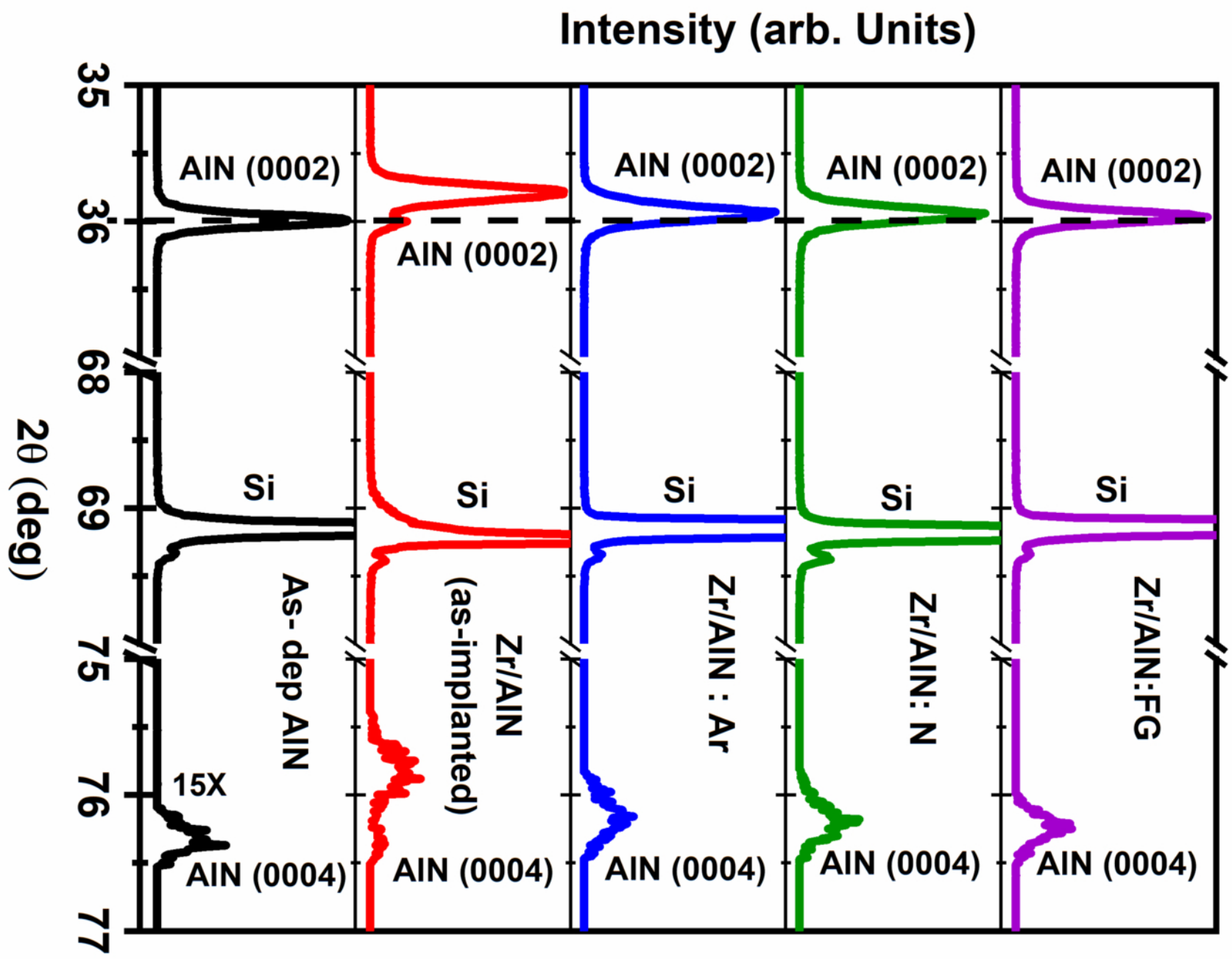

AIP Publishing

Journal of Applied Physics

ACCEPTED MANUSCRIPT

This is the author's peer reviewed, accepted manuscript. However, the online version of record will be different from this version once it has been copyedited and typeset.
PLEASE CITE THIS ARTICLE AS DOI: 10.1063/5.0030221

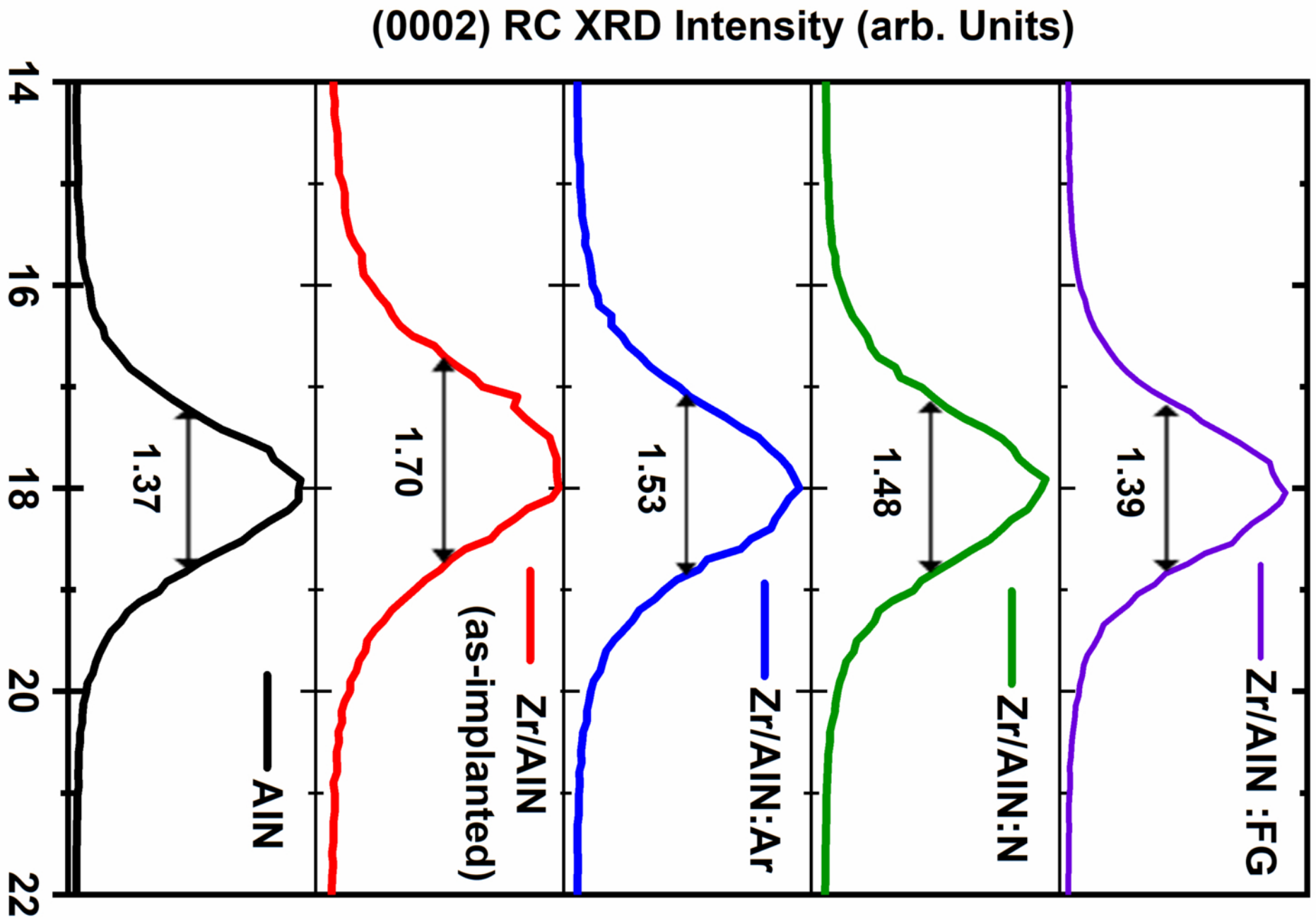

AIP Publishing

Journal of Applied Physics

ACCEPTED MANUSCRIPT

This is the author's peer reviewed, accepted manuscript. However, the online version of record will be different from this version once it has been copyedited and typeset.
PLEASE CITE THIS ARTICLE AS DOI: 10.1063/5.0030221

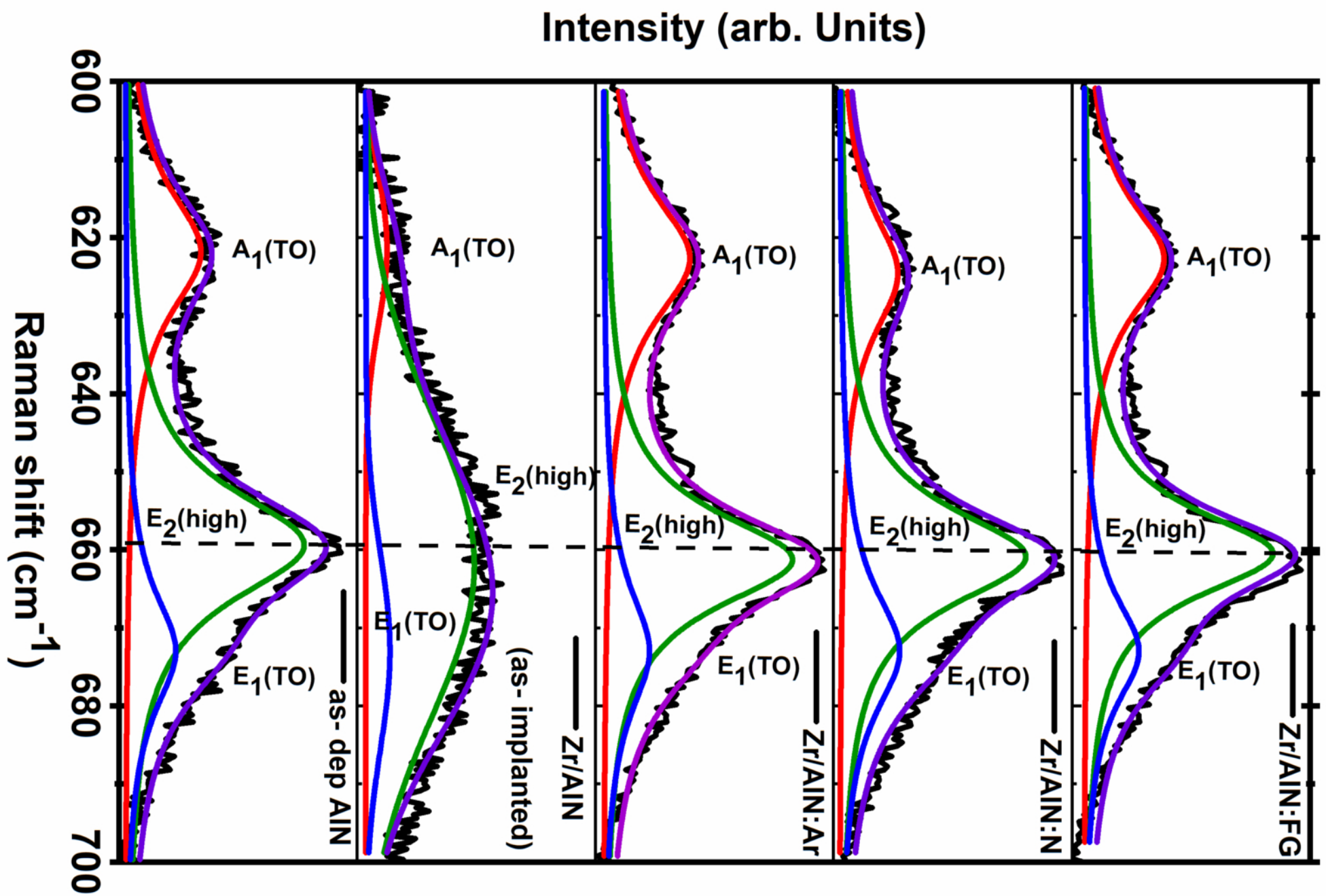

AIP Publishing

Journal of Applied Physics

ACCEPTED MANUSCRIPT

This is the author's peer reviewed, accepted manuscript. However, the online version of record will be different from this version once it has been copyedited and typeset.
PLEASE CITE THIS ARTICLE AS DOI: 10.1063/5.0030221

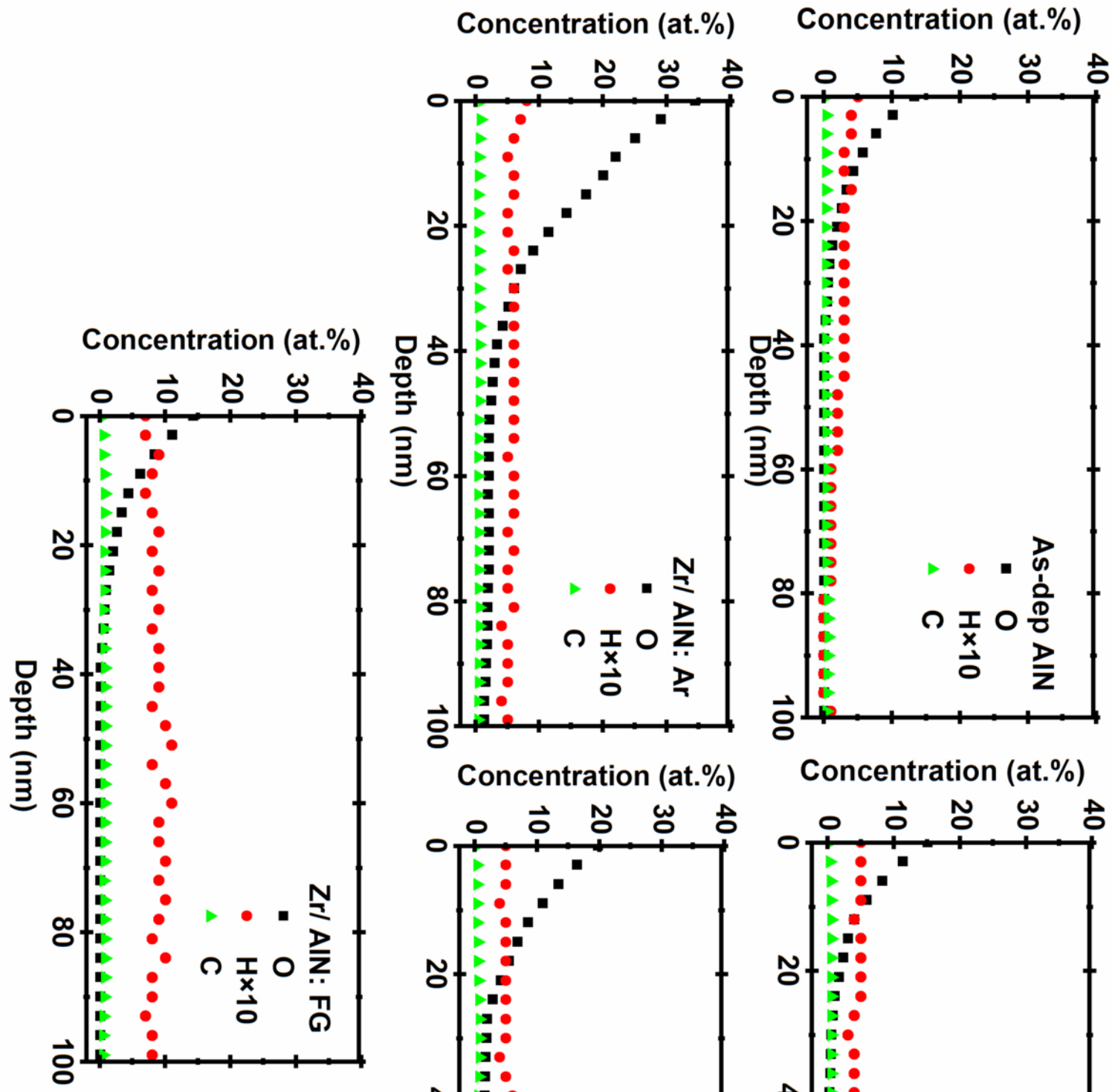

AIP Publishing

Journal of Applied Physics

ACCEPTED MANUSCRIPT

This is the author's peer reviewed, accepted manuscript. However, the online version of record will be different from this version once it has been copyedited and typeset.
PLEASE CITE THIS ARTICLE AS DOI: 10.1063/5.0030221

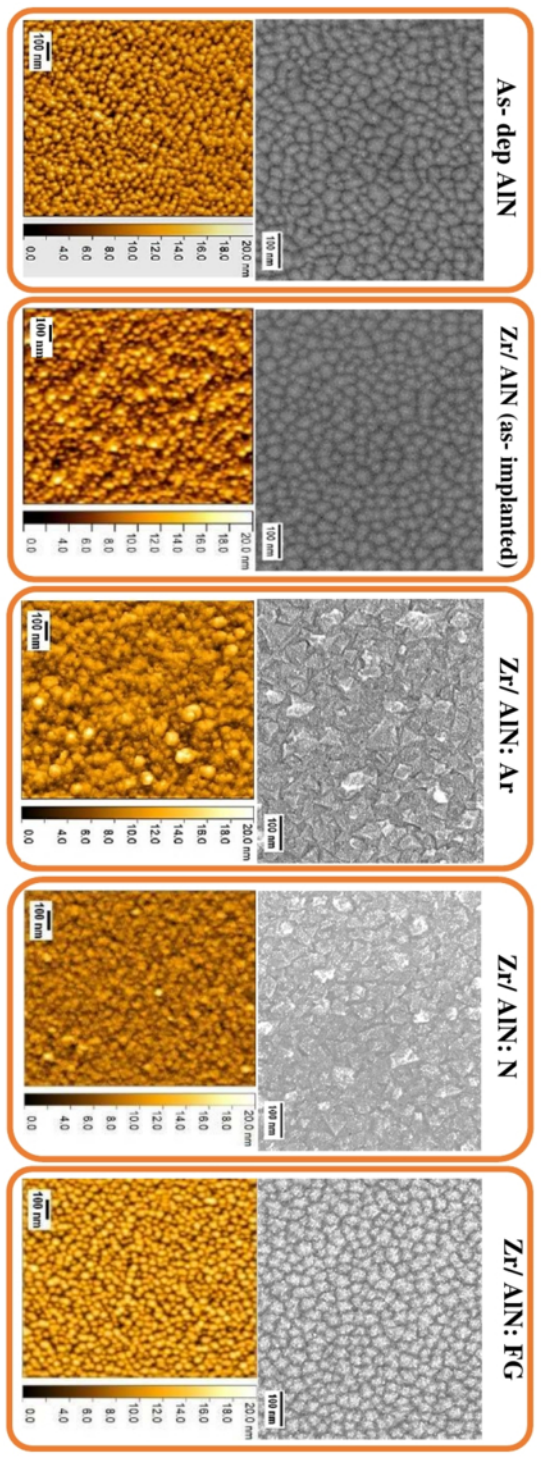

AIP Publishing

Journal of Applied Physics

ACCEPTED MANUSCRIPT

This is the author's peer reviewed, accepted manuscript. However, the online version of record will be different from this version once it has been copyedited and typeset.
PLEASE CITE THIS ARTICLE AS DOI: 10.1063/5.0030221

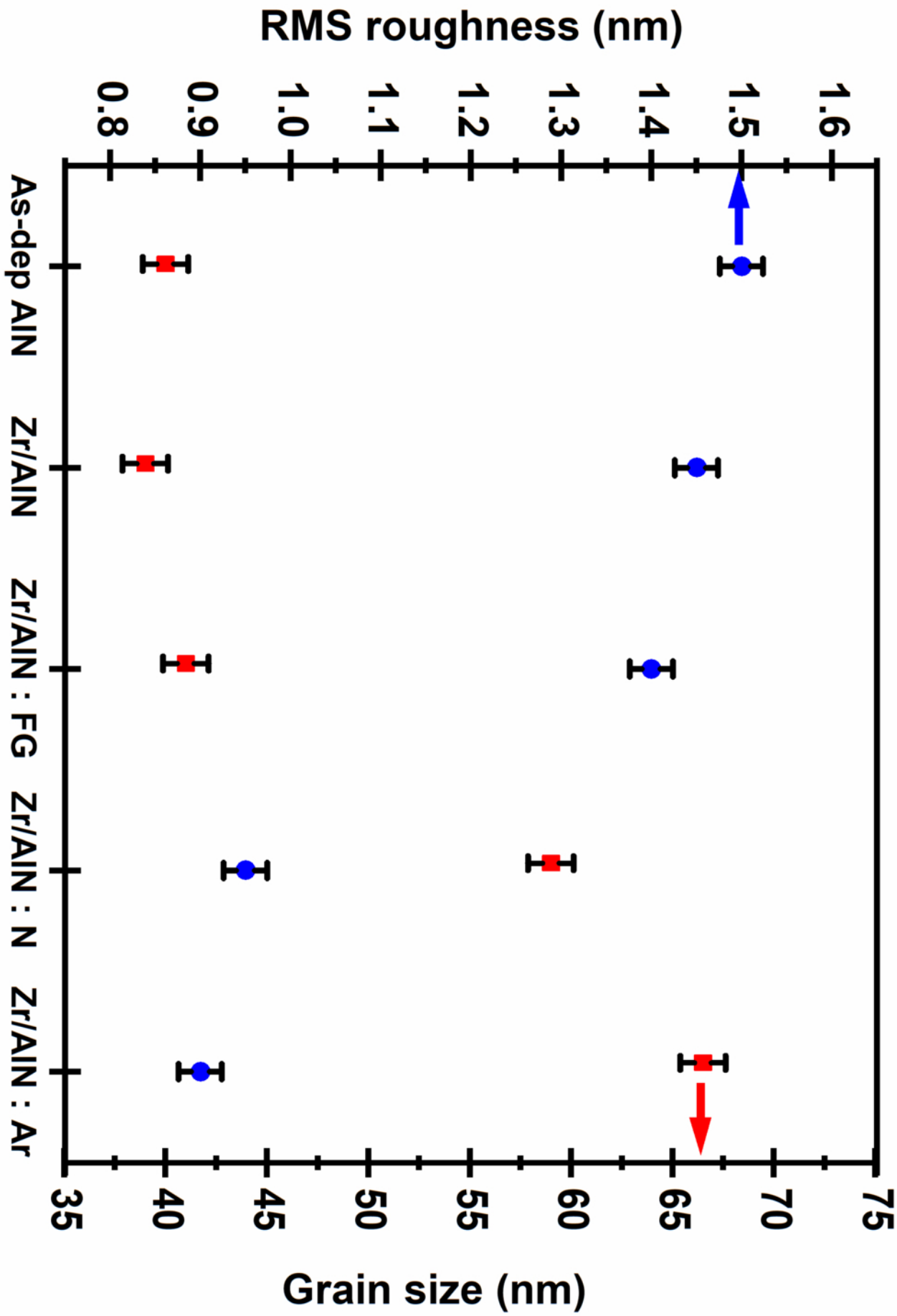

AIP Publishing

Journal of Applied Physics

ACCEPTED MANUSCRIPT

PLEASE CITE THIS ARTICLE AS DOI: 10.1063/5.0030221

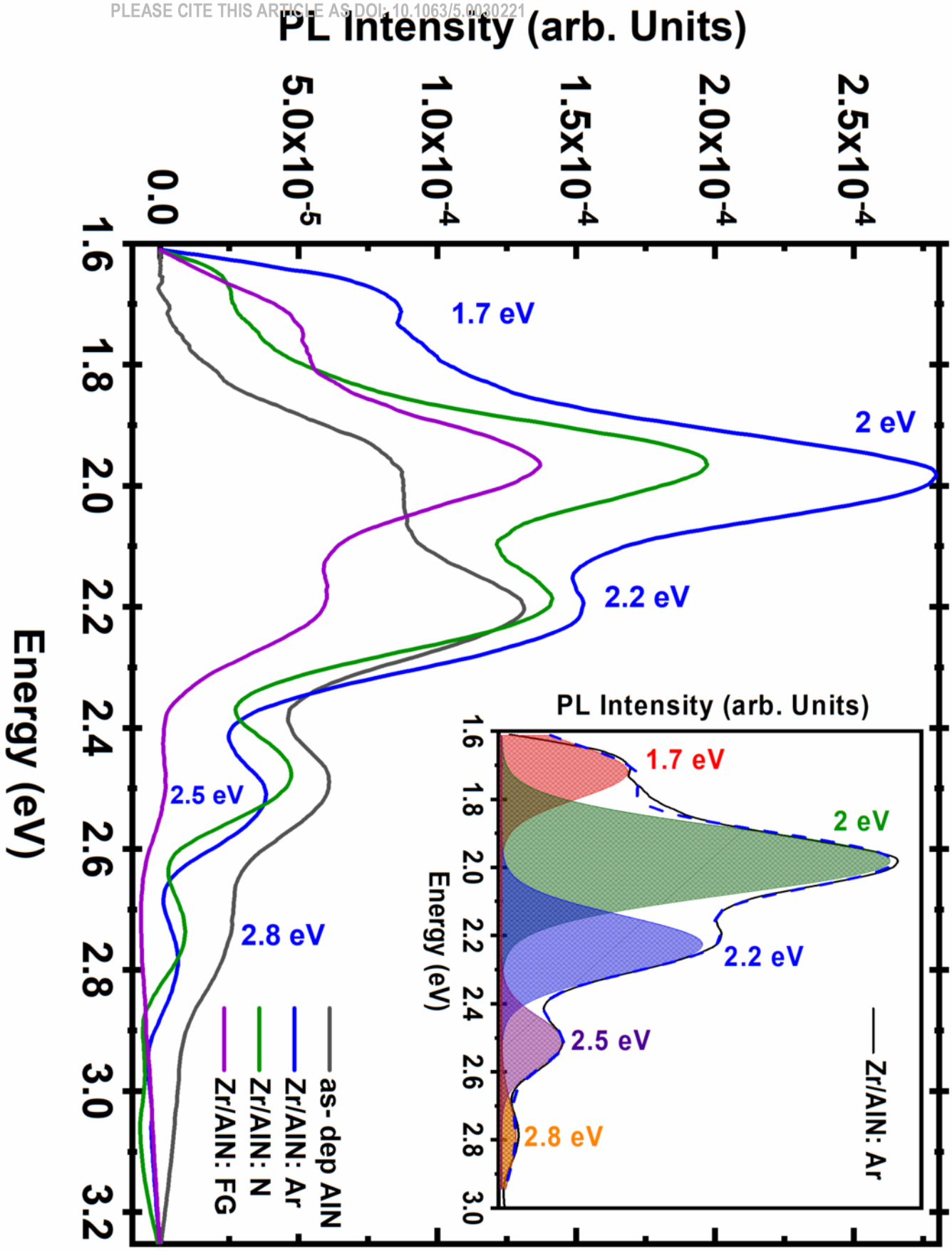

Journal of Applied Physics

ACCEPTED MANUSCRIPT

This is the author's peer reviewed, accepted manuscript. However, the online version of record will be different from this version once it has been copyedited and typeset.
PLEASE CITE THIS ARTICLE AS DOI: 10.1063/5.0030221